

PAPER

Zonal flow generation and toroidal Alfvén eigenmode excitation due to tearing mode induced energetic particle redistribution

To cite this article: H.W. Zhang *et al* 2022 *Nucl. Fusion* **62** 026047

View the [article online](#) for updates and enhancements.

You may also like

- [MHD modelling of density limit disruptions in tokamaks](#)
A. Bondeson, R.D. Parker, M. Hugon et al.
- [Influence of low-Z impurity on the stabilization of \$m/n = 2/1\$ tearing/locked modes in EAST](#)
Ming Xu, YunFeng Liang, Lai Wei et al.
- [Experimental observations of an \$n = 1\$ helical core accompanied by a saturated \$m/n = 2/1\$ tearing mode with low mode frequencies in JT-60U](#)
T Bando, G Matsunaga, M Takechi et al.

Zonal flow generation and toroidal Alfvén eigenmode excitation due to tearing mode induced energetic particle redistribution

H.W. Zhang^{ID}, Z.W. Ma^{*}^{ID}, J. Zhu, W. Zhang and Z.Y. Qiu^{ID}

Institute for Fusion Theory and Simulation, Department of Physics, Zhejiang University, Hangzhou 310027, People's Republic of China

E-mail: zwma@zju.edu.cn

Received 13 August 2021, revised 30 November 2021

Accepted for publication 7 December 2021

Published 12 January 2022



Abstract

Generation of the $n = 0$ zonal flow and excitation of the $n = 1$ toroidal Alfvén eigenmode (TAE) due to the redistribution of energetic particles (EPs) by the $m/n = 2/1$ tearing mode (TM) are systematically studied with the hybrid drift-kinetic magnetohydrodynamic (MHD) simulations (m and n represent the poloidal and toroidal mode number, respectively). In the presence of the $m/n = 2/1$ TM, the amplitude of the $n = 1$ TAE shows a slower decay after its first saturation due to the wave–particle nonlinearity and the nonlinear generation of the $n = 0$ & higher- n ($n \geq 2$) sidebands. Meanwhile, a strong $n = 0$ zonal flow component is nonlinearly generated when both TAE and TM grow to large amplitudes. The redistribution of EPs by the $m/n = 2/1$ magnetic island results in a continuous drive on the background plasma, and finally produces the zonal flow through the MHD nonlinearity. In addition, the large $m/n = 2/1$ magnetic island is found to be responsible for the formation of the strong spatial gradient of the EP distribution through the resonance between EPs and TM, which can lead to burst of unstable TAE and destabilization of originally stable TAE.

Keywords: toroidal Alfvén eigenmode, tearing mode, energetic particle, zonal flow

(Some figures may appear in colour only in the online journal)

1. Introduction

Energetic particles (EPs) and their interactions with magnetohydrodynamic (MHD) modes are important issues in burning plasmas of future reactors. For example, Alfvén eigenmodes (AEs) destabilized by EPs through inverse Landau damping may effectively modify the EP distribution and influence the overall plasma confinement [1]. Representative, the toroidal Alfvén eigenmodes (TAEs) existing in the continuum gap associated with the toroidicity in Tokamaks can be much easily destabilized by EPs [2, 3], and have been intensively studied as a paradigm of shear Alfvén wave instabilities. On the

other hand, tearing mode (TM) instabilities also often exist in tokamak plasmas, which can significantly change the magnetic topology and convert the magnetic energy into the kinetic energy of the plasma. The interactions between TMs and EPs are investigated in recent works, including the influences of EPs on the linear stabilities of TMs [4–8], the resonance conditions between EPs and TMs [8, 9], and the transitions from TMs to energetic particle modes (EPMs) due to resonant excitations [7, 9]. In addition, the interactions/couplings between AEs and TMs are also observed frequently in tokamak experiments and have been widely studied [10–17].

In a previous simulation study adopting the hybrid drift-kinetic MHD code (CLT-K), the nonlinear interaction between the $n = 1$ TAE and the $m/n = 2/1$ TM was investigated (m and n represent the poloidal and toroidal mode number, respectively.) [17]. It was found that the enhanced TM activities

* Author to whom any correspondence should be addressed.

weaken the frequency chirping of TAE through the nonlinear interaction between passing EPs resonating with TAE and TM in the phase space. The simulation results also indicated that the $n = 0$ zonal component is indispensable for the saturation of TM. Besides, a dominant $n = 0$ zonal flow component is generated with both saturated TAE and TM at the end of the simulation, while the underlying mechanism is not well understood yet.

It is well accepted that zonal flows can suppress the anomalous turbulent transport and largely improve the plasma confinement [18, 19], due to their effectiveness in absorbing energy from drift waves including drift Alfvénic waves, and in suppressing turbulence through $\mathbf{E} \times \mathbf{B}$ shearing. According to the well-known paradigm of drift wave-zonal flow turbulence [20, 21], the modification of the drift wave turbulence by zonal flows is achieved by the nonlinear zonal flow generation through the self-organization processes driven by turbulences. The zonal flow generation can also be affected by EPs through different processes. For instance, a fine structure of the radial zonal electric field E_r due to the orbit loss of EPs caused by fishbone was measured in CHS [22].

Zonal flows are also regarded as one of the essential candidates for the nonlinear saturation of TAEs [23, 24], and have been studied both theoretically and numerically, including the reductions in the TAE saturation level due to generations of both the zero frequency zonal flow [17, 18] as well as the finite frequency geodesic acoustic mode [19, 20], in which EPs may play a significant role. It is noteworthy that, in the hybrid simulation by the MEGA code [23], the dissipations from the sidebands (the $n = 0$ zonal component and the higher- n modes with $n \geq 8$) of the principal $n = 4$ TAE were found to be effective in reducing the saturation amplitude of TAE by half when $\delta B_r/B \sim 10^{-2}$. The growth rate of the $n = 0$ zonal component is twice that of the $n = 4$ component at the linear stage of TAE, which was explained theoretically in reference [24], based on the forced driven generation of the zonal flow due to the EP induced coupling.

In this paper, we report the CLT-K simulation results of the nonlinear interaction between the $n = 1$ TAE and the $m/n = 2/1$ TM. In the presence of TM, the amplitude of TAE shows a slower decay after its first saturation due to the wave-particle interaction and the nonlinear generation of the $n = 0$ & higher- n ($n \geq 2$) sidebands. Meanwhile, a strong $n = 0$ zonal flow component is nonlinearly generated after the saturation of both TAE and TM. The generation mechanism of the strong $n = 0$ zonal flow in the presence of both the $m/n = 2/1$ TM and the $n = 1$ TAE will be discussed in detail. In addition, an obvious EP redistribution by the saturated $m/n = 2/1$ magnetic island is observed, which results in burst of unstable TAE and destabilization of originally stable TAE.

The outline of the present paper is organized as follows: Section 2 introduces the simulation model and parameters used in the CLT-K code; section 3 presents the simulation results and analyzes the nonlinear interaction between TAE and TM; and finally, the results of the present paper are summarized in section 4.

2. Simulation model and parameters

2.1. Overview of the CLT-K code

In the CLT-K code, to describe the background plasma, we solve the full set of single fluid, resistive MHD equations including dissipations in the (R, φ, Z) cylindrical coordinate [25–31], i.e.

$$\partial_t \rho = -\nabla \cdot (\rho \mathbf{v}) + \nabla \cdot [D \nabla (\rho - \rho_0)], \quad (1)$$

$$\partial_t p = -\mathbf{v} \cdot \nabla p - \Gamma p \nabla \cdot \mathbf{v} + \nabla \cdot [\kappa \nabla (p - p_0)], \quad (2)$$

$$\partial_t \mathbf{v} = -\mathbf{v} \cdot \nabla \mathbf{v} + (\mathbf{J} \times \mathbf{B} - \nabla p) / \rho + \nabla \cdot [\nu \nabla (\mathbf{v} - \mathbf{v}_0)], \quad (3)$$

$$\partial_t \mathbf{B} = -\nabla \times \mathbf{E}, \quad (4)$$

with

$$\mathbf{E} = -\mathbf{v} \times \mathbf{B} + \eta (\mathbf{J} - \mathbf{J}_0), \quad (5)$$

$$\mathbf{J} = \nabla \times \mathbf{B}, \quad (6)$$

where ρ , p , \mathbf{v} , \mathbf{B} , \mathbf{E} , and \mathbf{J} are the plasma density, thermal pressure, plasma velocity, magnetic field, electric field, and current density, respectively. The subscript ‘0’ denotes equilibrium quantities. $\Gamma (=5/3)$ is the ratio of specific heat of the plasma. The following normalization will be used throughout the whole paper and therefore the units are omitted: $\mathbf{B}/B_{00} \rightarrow \mathbf{B}$, $\mathbf{x}/a \rightarrow \mathbf{x}$, $\rho/\rho_{00} \rightarrow \rho$, $\mathbf{v}/v_A \rightarrow \mathbf{v}$, $t/\tau_A \rightarrow t$, $p/(B_{00}^2/\mu_0) \rightarrow p$, $\mathbf{J}/(B_{00}/\mu_0 a) \rightarrow \mathbf{J}$, $\mathbf{E}/(v_A B_{00}) \rightarrow \mathbf{E}$, $\eta/(\mu_0 v_{AA}) \rightarrow \eta$, and $D, \kappa, \nu/(v_A a) \rightarrow D, \kappa, \nu$, where a is the minor radius in the poloidal cross-section, $v_A = B_{00}/\sqrt{\mu_0 \rho_{00}}$ is the Alfvén speed at the magnetic axis, $\tau_A = a/v_A$ is the Alfvén time, and the Alfvén frequency is $\omega_A = v_A/a$. The frequency ω and the growth rate γ of modes are normalized by ω_A . B_{00} and ρ_{00} are the initial magnetic field strength and plasma mass density at the magnetic axis, respectively. The normalized radial coordinate r will be used, where $r = \psi_n^{1/2}$, and ψ_n is the normalized poloidal flux. Recently, benchmarks between the CLT code and the M3D-C1 code for the $m/n = 2/1$ resistive TM and the $m/n = 1/1$ resistive kink mode have been performed (without EPs), which confirms the consistencies of the linear and nonlinear results simulated with the two MHD codes [32].

In the hybrid drift-kinetic MHD model, the effects of EPs are coupled into the momentum equation through the EP current \mathbf{J}_h or the EP pressure tensor \mathbf{P}_h [33], i.e.

$$\partial_t \mathbf{v} = -\mathbf{v} \cdot \nabla \mathbf{v} + [(\mathbf{J} - \mathbf{J}_h) \times \mathbf{B} - \nabla p] / \rho + \nabla \cdot [\nu \nabla (\mathbf{v} - \mathbf{v}_0)], \quad (7)$$

$$\begin{aligned} \partial_t \mathbf{v} = & -\mathbf{v} \cdot \nabla \mathbf{v} + [\mathbf{J} \times \mathbf{B} - \nabla p - (\nabla \cdot \mathbf{P}_h)_\perp] / \rho \\ & + \nabla \cdot [\nu \nabla (\mathbf{v} - \mathbf{v}_0)], \end{aligned} \quad (8)$$

where the subscript ‘ h ’ denotes EPs. The term $Z_h e \mathbf{E}$ (Z_h is the charge number of EPs and e is the charge unit) does not appear in equation (7) because it counteracts the contribution of $\mathbf{E} \times \mathbf{B}$ drift in the EP current. In the previous investigations

with the CLT-K code [17, 31], the current coupling scheme was adopted. Recently, the pressure coupling scheme has been included in the latest version of the CLT-K code. As shown in figure 6, the results of the two coupling schemes are almost identical in the linear and nonlinear phases. A more detailed comparison and benchmark study between the current and pressure coupling schemes will be discussed in a near-future work.

To advance the EPs' orbits, we adopt the five-dimensional guiding-center equations of motion [34], i.e.

$$\frac{d\mathbf{X}}{dt} = \frac{1}{B_{\parallel}^*} [v_{\parallel} \mathbf{B}^* + \mathbf{E}^* \times \mathbf{b}], \quad (9)$$

$$\frac{dv_{\parallel}}{dt} = \frac{Z_h e}{m B_{\parallel}^*} \mathbf{B}^* \cdot \mathbf{E}^*, \quad (10)$$

where $\mathbf{B}^* = \nabla \times \mathbf{A}^*$, $B_{\parallel}^* = \mathbf{B}^* \cdot \mathbf{b}$, (\mathbf{b} is the unit vector of the magnetic field), and $\mathbf{E}^* = -\nabla \Phi^* - \partial_t \mathbf{A}^*$. The effective electric and magnetic vector potentials Φ^* and \mathbf{A}^* are:

$$\Phi^* = \Phi + \frac{1}{Z_h e} \mu B, \quad (11)$$

$$\mathbf{A}^* = \mathbf{A} + \frac{mv_{\parallel}}{Z_h e} \mathbf{b}. \quad (12)$$

The μ , Φ and \mathbf{A} are respectively the magnetic moment, the electric potential, and the magnetic vector potential.

The EP current \mathbf{J}_h in equation (7) mainly consists of two components: the guiding center current \mathbf{J}_{GC} and the magnetization current \mathbf{J}_{MAG} :

$$\mathbf{J}_h = \mathbf{J}_{GC} + \mathbf{J}_{MAG}, \quad (13)$$

where

$$\mathbf{J}_{GC} = \int Z_h e (\mathbf{v}_{\text{curvature}} + \mathbf{v}_{\nabla B} + \mathbf{v}_B) f dv^3, \quad (14)$$

$$\mathbf{v}_{\text{curvature}} = \frac{mv_{\parallel}^2}{Z_h e B_{\parallel}^*} \nabla \times \mathbf{b}, \quad (15)$$

$$\mathbf{v}_{\nabla B} = \frac{\mu}{Z_h e B_{\parallel}^*} \mathbf{b} \times \nabla B, \quad (16)$$

$$\mathbf{v}_B = v_{\parallel} \frac{\mathbf{B}}{B_{\parallel}^*}, \quad (17)$$

and

$$\mathbf{J}_{MAG} = \nabla \times \mathcal{M} = -\nabla \times \int \mu \mathbf{b} f dv^3. \quad (18)$$

The EP pressure tensor \mathbf{P}_h is expressed in the Chew–Goldberger–Low (CGL) form [35]:

$$\mathbf{P}_h = P_{h\perp} \mathbf{I} + (P_{h\parallel} - P_{h\perp}) \mathbf{b} \mathbf{b}, \quad (19)$$

where \mathbf{I} is the unit tensor, and (M in the following equations is the mass of EPs)

$$P_{h\perp} = \int \frac{1}{2} M v_{\perp}^2 f dv^3, \quad (20)$$

$$P_{h\parallel} = \int M v_{\parallel}^2 f dv^3. \quad (21)$$

To reduce the noise in particle-in-cell (PIC) simulations, the δf method [31, 36, 37] is used to evolve the distribution

function of EPs. We also ignore the contribution of EPs on equilibrium, that is, only the perturbed $\delta \mathbf{J}_h$ or $\delta \mathbf{P}_h$ according to equations (13)–(21) is included in the simulations.

2.2. Simulation parameters and the initial equilibrium

A mesh consisting of $200 \times 16 \times 200$ points in (R, φ, Z) is utilized for all cases, including about 40 markers in each grid cell. The numerical convergence has been verified. The isotropic slowing down distribution for EPs is chosen:

$$f_0 = \frac{1}{v^3 + v_c^3} \left[1 + \text{erf} \left(\frac{v_0 - v}{\Delta v} \right) \right] \exp \left(-\frac{\langle \psi \rangle}{\Delta \psi} \right), \quad (22)$$

with $v_c = 0.5v_A$, $v_0 = 1.2v_A$, $\Delta v = 0.2v_A$, $\Delta \psi = 0.37(\psi_{\max} - \psi_{\min})$, and $\langle \psi \rangle$ is the averaged poloidal flux over the particle orbit [31]. The initial profiles of the radial distribution and the radial gradient of EPs are plotted in figure 1(a). The steepest gradient region of the radial distribution of EPs is at $r \approx 0.43$. The Larmor radius ρ_h of the EP with the perpendicular speed of v_0 is equal to $0.12a$. The beta of EPs at the magnetic axis β_h^c ranges from 0.7%–2.34%, which will be annotated clearly for each simulation case. The resistivity values used are $\eta = 10^{-7}$ and 10^{-5} for the cases without and with the TM, respectively. The dissipations coefficients are $D, \kappa \& \nu = 3.2 \times 10^{-6}$.

In the present simulations, we choose a zero beta ($\beta_b = 0$) tokamak equilibrium constructed from the QSOLVER code [38] with shifted circular flux surfaces and an aspect ratio $R_0/a = 3.2$. The plasma density is assumed to be uniform. The initial safety factor profile is shown in figure 1(b). The instability parameter Δ' for the $m/n = 2/1$ TM is estimated to be 23.1 [39], indicating that the $m/n = 2/1$ TM is unstable. In this work, we focus on the $n = 1$ TAE and TM. Thus, only the $n = 1$ components of the perturbed $\delta \mathbf{J}_h$ and $\delta \mathbf{P}_h$ are considered in simulations.

3. Simulation results

3.1. Basic properties of the $m/n = 2/1$ TM and the $n = 1$ TAE

Firstly, we carry out a nonlinear simulation with only the $m/n = 2/1$ TM (**the pure TM case**). The resistivity used is $\eta = 10^{-5}$. The time evolution of the kinetic energy is given in figure 2. The $n = 1$ TM firstly grows linearly with the growth rate $\gamma = 0.0027$ and then saturates after $t = 8000$. As shown by the black dotted lines in figure 2, after the $n = 0$ component is filtered out in the simulation, the kinetic energy of TM will not saturate. Consequently, the perturbed $n = 0$ component, resulting from nonlinear coupling, plays an essential role in the saturation of TM, which is consistent with the previous simulation result [17]. Nevertheless, the $n = 0$ zonal component is still much weaker than the $n = 1$ TM component as shown by the colored solid lines in figure 2. The mode structure of the poloidal electric field E_θ and the Poincaré plot of magnetic field for the saturated TM are presented in figure 3. The mode shows a clear $m/n = 2/1$ TM structure and localizes around the $q = 2$ rational surface.

Secondly, a nonlinear $n = 1$ TAE simulation without TM (**the pure TAE case**) is performed with a lower resistivity

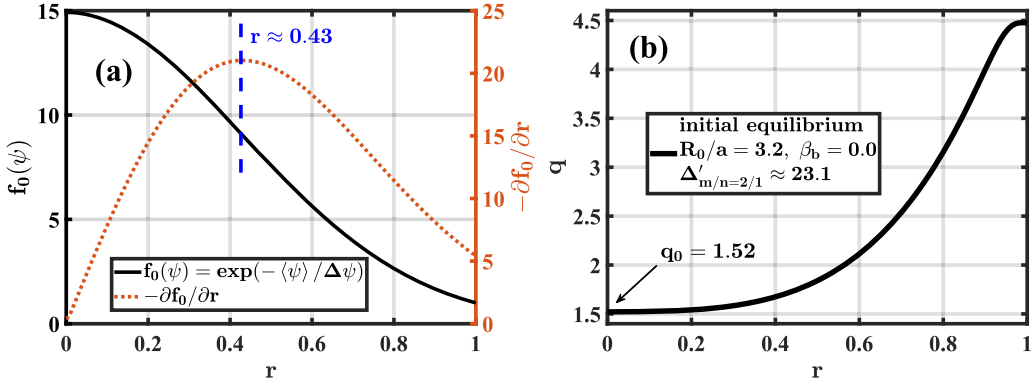


Figure 1. (a) Initial profiles of the radial distribution (solid line) and the radial gradient (dotted line) of EPs. The steepest gradient region of the radial distribution of EPs is marked out with the dashed line at $r \approx 0.43$. (b) Initial profile of the safety factor q .

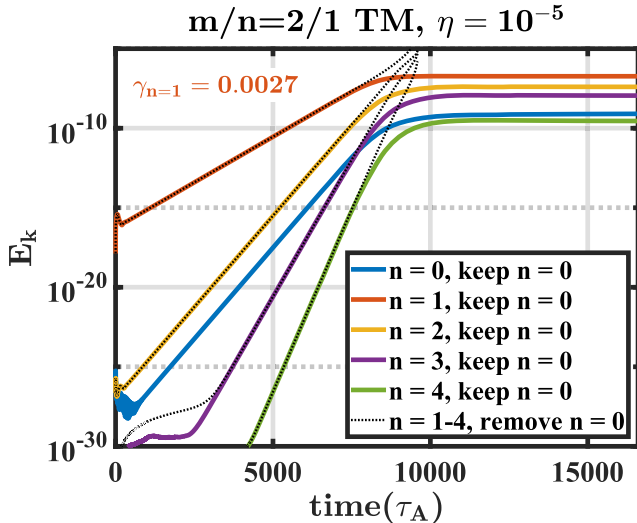


Figure 2. Time evolution of the kinetic energy for the simulation of the pure TM case. Colored solid lines present the results without filtering (i.e. the $n = 0$ component remains) while black dotted lines show the results that the $n = 0$ component is filtered out.

($\eta = 10^{-7}$) to reduce the growth rate of the resistive TM. Thus, the amplitude of the TM component in this pure TAE case is much less than that of the TAE component and the influence of TM can be ignored within the time scale of the simulation (less than $20\,000\tau_A$). The EP beta at the core is chosen to be $\beta_h^c = 2.34\%$. Figure 4(a) presents the time evolution of the kinetic energy of TAE. The growth rate of the $n = 0$ zonal component ($\gamma_{n=0} = 0.0229$) is about twice that of the $n = 1$ TAE component ($\gamma_{n=1} = 0.0115$) during the linear stage of TAE ($t < 3000$) due to the forced driven process of TAE, which is consistent with the previous simulation and theoretical studies [23, 24, 40]. After the saturation of TAE due to the wave-particle nonlinearity and the nonlinear generation of the $n = 0$ & higher- n ($n \geq 2$) sidebands, the amplitudes of both the $n = 0$ and $n = 1$ components decay to low levels as shown in figure 4(a). The saturation mechanism of the TAE is actually complicated, with several processes dominating in different parameter regimes, and has been systematically studied separately by previous researches. The former saturation

mechanism of TAE is mainly caused by the wave-particle trapping [41], which indicates the saturation amplitude of TAE should scale as $\delta E_{\text{sat}} \propto \gamma_L^2$ when the MHD nonlinearity is not included (δE_{sat} is the saturation amplitude of TAE, and γ_L is the linear growth rate of TAE). In our previous study with the CLT-K code [31], this scaling law was demonstrated in our simulation results for the $n = 1$ TAE. On the other hand, the $n = 0$ and higher- n ($n \geq 2$) sidebands significantly influence the saturation amplitude of TAE by spectral energy transfer, which has also been systematically studied by both numerical and theoretical investigations [23, 24, 40]. The amplitude decline of the primary $n = 1$ component is mainly resulted from the damping effects from the nonlinear coupled components, including the $n = 0$ zonal component and the higher- n ($n \geq 2$) sidebands [23, 24, 40]. The decay rate of the $n = 0$ zonal component plotted by blue solid lines in figures 4(a) and (b) is about -2.10×10^{-4} around $t = 11\,000$. To understand the damping mechanism of the $n = 0$ component, we separate out the $n = 0$ component of the viscous term in the momentum equation, i.e. the viscous term becomes $\nabla \cdot [\nu^{n=0} \nabla (\mathbf{v}^{n=0} - \mathbf{v}_0)] + \nabla \cdot [\nu \nabla (\mathbf{v}^{n \geq 1})]$, and then the viscosity for the $n = 0$ viscous term is quintupled ($\nu^{n=0} = 5\nu$) in the pure TAE case after $t = 10\,370$. As shown by black dotted lines in figure 4(b), we find the decay rate of the $n = 0$ kinetic energy increases to -1.06×10^{-3} with the increased $\nu^{n=0}$, which is about five times as large as the original decay rate. Thus, the viscous term in the momentum equation is a dominant damping factor influencing the decay rate of the $n = 0$ zonal component after its saturation. In figure 5(a), the frequency of the $n = 1$ TAE at its linear stage ($\omega_{\text{TAE}} \approx 0.053$) localizes in the TAE gap of the $n = 1$ shear Alfvén continuum, but the mode also intersects the $m = 2$ continuum at $r \approx 0.4$ and forms the $m = 2$ EPM component. The typical Larmor radius of EPs (with the perpendicular speed of v_0) in the simulation is $0.12a$, and EPs also exist at the coupling position of the $m = 2$ EPM component and the shear Alfvén continuum. Consequently, any sharp structures smaller than or comparable to the EP drift orbit width are resolved by finite orbit width effects of EPs and the mode structure of the $m = 2$ EPM component in figure 5(b) is not sharp as it couples the shear Alfvén continuum at $r \approx 0.4$. The mode structure in figures 5(b) and

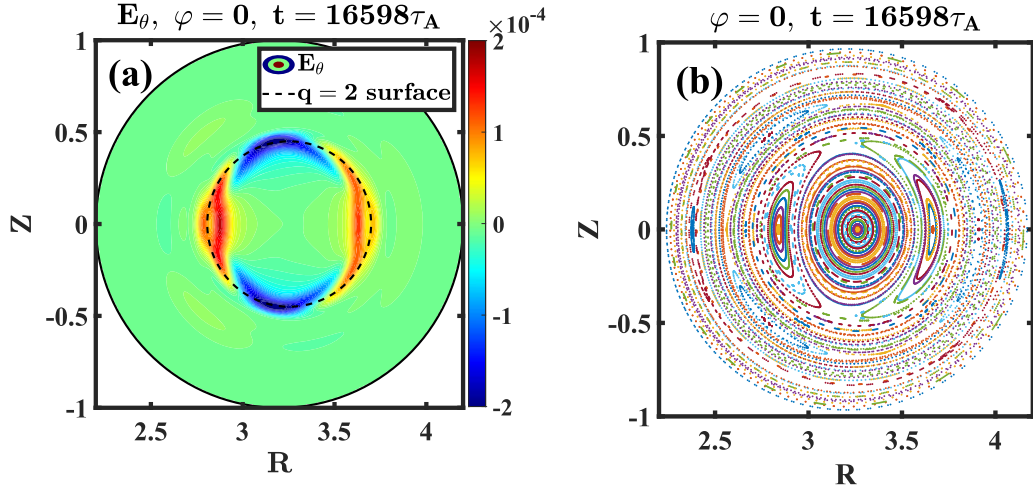


Figure 3. (a) Contour plot of the poloidal electric field E_θ and (b) Poincaré plot of magnetic field for the $m/n = 2/1$ TM at the saturation stage.

(c) mainly consists of the $m = 2$ and 3 harmonics. Nevertheless, the amplitude of its $m = 2$ harmonic intersecting the $m = 2$ continuum in figure 5(b) is larger than that of both the $m = 2$ and $m = 3$ harmonics in the region of the TAE gap, which is mainly caused by the large radial gradient of the EP distribution at $r \approx 0.4$ as shown in figure 1(a). Consequently, the $m = 2$ harmonic of the mode in figure 5 is contributed from both TAE and EPM. Since the mode frequency falls within the TAE gap and the global mode structure consists of $m = 2$ & 3 harmonics, this mode will be defined as TAE for simplicity.

3.2. Nonlinear interaction between the $m/n = 2/1$ TM and the $n = 1$ TAE

In this subsection, we carry out a nonlinear hybrid simulation with both TM and TAE to study the nonlinear interaction between the $m/n = 2/1$ TM and the $n = 1$ TAE (**the TAE + TM case**). The resistivity and the EP beta are respectively the same as the pure TM case ($\eta = 10^{-5}$) and the pure TAE case ($\beta_h^c = 2.34\%$). Compared with the pure TAE case in figure 4(a) ($\eta = 10^{-7}$, $\gamma = 0.0115$), the TAE with larger resistivity has a smaller growth rate ($\eta = 10^{-5}$, $\gamma = 0.00875$), as shown in figure 6. For the TAE + TM case, the system has experienced three saturation processes: firstly, the TAE saturates due to the nonlinear wave-particle interaction [31, 41] and the nonlinear generation of the $n = 0$ & higher- n ($n \geq 2$) sidebands [23, 24, 40] around $t = 3300$. Secondly, the TM starts to saturate mainly due to the generation of the $n = 0$ zonal component through the nonlinear mode coupling around $t = 8000$ as shown in figure 2. In the meantime, the $n = 0$ zonal flow component shows a secondary growth during the saturation stage of the TM. Finally, all modes including the $n = 0$ zonal flow are saturated after $t = 15000$. The $n = 0$ component eventually becomes dominant, which is even an order of magnitude larger in the amplitude than the $n = 1$ components of TAE & TM. For the $n = 1$ component, the final saturated amplitudes of the low-frequency TM and the high-frequency TAE are comparable, as will be shown in figure 8(a). In addition, as shown in

figure 6, the exactly same results can be obtained via both the pressure coupling and current coupling schemes. The generation mechanism of the dominant $n = 0$ zonal flow component will be explained in the next subsection.

The influence of TM on the time evolution of TAE is shown in figure 7. The real component of the poloidal electric field of TAE ($E_{\theta,\text{norm}}^{m/n=2/1}$) at the $q = 2.49$ surface is plotted after normalization by its maximum value. In comparison with the pure TAE case, the obvious difference made by TM is that TAE has a longer decay time and a relatively larger saturation amplitude after $t = 4000$. The larger TAE saturation level with TM is associated with the redistribution of EPs due to the $m/n = 2/1$ magnetic island, which will be demonstrated in the next section in detail. For TM, the presence of EPs results in a finite low frequency of TM in the direction of ion diamagnetic drift. At the linear stage of TM, the frequency of TM is approximately equal to 0.0009. While in the nonlinear stage of TM, the frequency of TM drops to zero due to the flattening of the EP distribution around the $q = 2$ rational surface. The radial mode structures (E_θ) of the high-frequency $n = 1$ TAE at the nonlinear stage are plotted by solid lines in figure 8. For the TAE + TM case in figure 8(a), the $n = 1$ high-frequency TAE mode structure is separated out with a high-pass filter ($\omega \geq 0.002$), i.e. the remaining low-frequency ($\omega < 0.002$) component is dominated by the TM. The $m = 2$ mode structure of the low-frequency $m/n = 2/1$ TM in the TAE + TM case is plotted by the dotted line in figure 8(a). As we can see, the $m = 2$ component of the low-frequency TM is comparable in magnitude with that of the high-frequency TAE in figure 8(a). It is evident that in the presence of TM, the mode structure of TAE becomes wide and flat, and the $m = 2$ harmonic becomes much larger than the $m = 3$ & 4 harmonics as shown in figure 8(a). The broad mode structure in figure 8(a) is mainly caused by the redistribution of EPs by TM, which results in an enhancement of the radial gradient of the EP distribution in a wide radial range, as will be demonstrated in section 3.4. Furthermore, the strong and sheared zonal flow leads to a significant flattening and reduction on the $m = 3$ harmonic of TAE

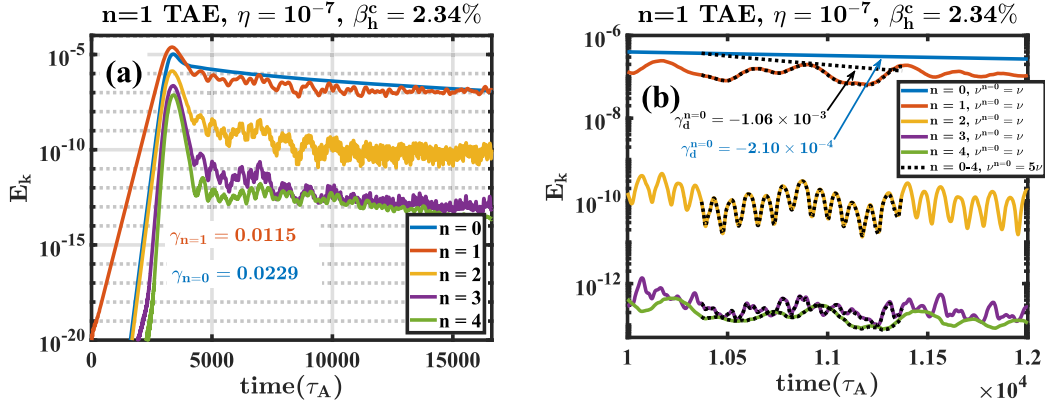


Figure 4. (a) Time evolution of the kinetic energy for the simulation of the pure TAE case; (b) colored solid lines are the enlargement of (a), and black dotted lines represent the evolution of kinetic energy with the increased viscosity for the $n = 0$ viscous term, i.e. $\nu^{n=0} = 5\nu$ after $t = 10\,370$. The decay rates of the $n = 0$ components ($\gamma_d^{n=0}$) are annotated in (b) for cases with different $\nu^{n=0}$.

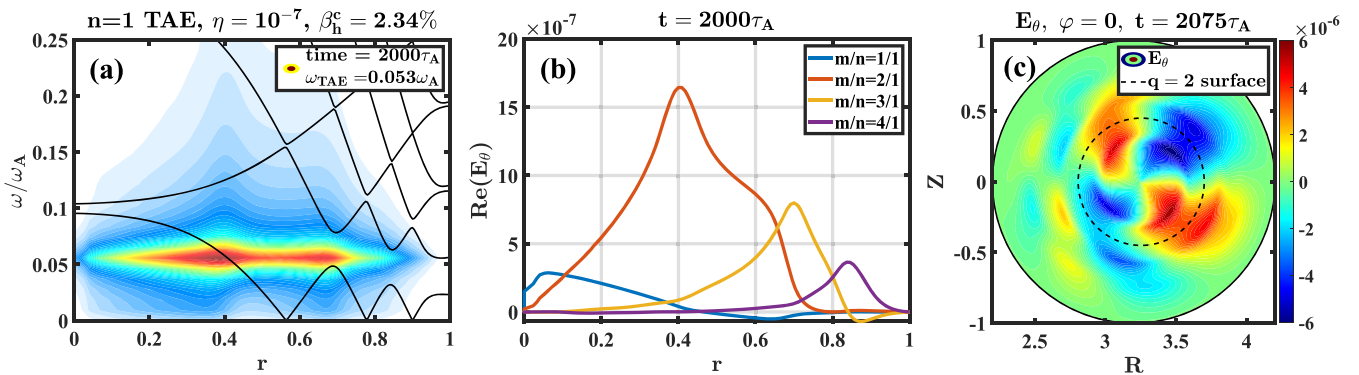


Figure 5. (a) Frequency distribution of the $n = 1$ TAE (E_θ) with the $n = 1$ shear Alfvén continuum (solid lines), (b) radial mode structures (real component), and (c) contour plot of the poloidal electric field E_θ for the $n = 1$ TAE at the linear stage.

in figure 8(a). While for the pure TAE case in figure 8(b), the $n = 1$ mode structure is much sharper and the amplitudes of the $m = 3$ & 4 harmonics are much larger than those in the TAE + TM case in figure 8(a).

To further understand the resonances between EPs and the modes, we plot the δf structures of EPs for the TAE + TM case for different pitch angles ($\Lambda = \mu B_0/E$). The wave-particle resonance condition is determined by: $\omega + p\omega_\theta - n\omega_\varphi = 0$, where ω_φ and ω_θ are the toroidal orbit frequency and the poloidal orbit frequency, respectively. The p is an integer with $p = l + m$, and the integer l is the Fourier harmonic of the poloidal motion of particles [31, 42]. As shown in figure 9, the $p = 1$ component of co-passing EPs (corresponding to $m = 2, l = -1$, and $\omega = 0.053$) and the $p = 0$ component of trapped EPs (corresponding to $m = 2, l = -2$, and $\omega = 0.053$) are mainly responsible for the wave-particle resonances to excite the $n = 1$ TAE (the same resonance conditions of EPs with TAE exist during the linear growth stage of TAE, which will not be repeated here). The fulfillment of the $p = 2$ TAE resonance condition (corresponding to $m = 3, l = -1$, and $\omega = 0.053$) is only found in the δf structure of co-passing EPs with small pitch angles ($\Lambda = 0$). For the $m/n = 2/1$ TM, the $p = 2$ resonance condition is clearly satisfied for co-passing EPs in figures 9(a) and (b) (corresponding to $m = 2, l = 0$, and

$\omega = 0.0$) [8, 9, 17]. However, no obvious resonance between the TM and trapped EPs is observed in figure 9(c).

3.3. Generation mechanisms of the dominant $n = 0$ zonal flow component

In this subsection, we will focus on analyzing the generation mechanisms of the dominant $n = 0$ zonal flow component in the TAE + TM case. Firstly, we analyze the mode frequencies and the time evolution properties of the TAE + TM case in figure 10. Note that the frequency spectra before $t = 2000$ are not plotted here because the amplitudes of TAE, TM, and zonal flow are too weak. As can be seen in figure 10(a), TAE is firstly excited by EPs with obvious upward and downward frequency chirpings. As TM grows to be significant ($t > 7000$), the significant $n = 0$ zonal flow component with zero-frequency is generated, see $E_r^{n=0}$ in figure 10(b). (The mode structure of $E_r^{n=0}$ is almost the same as the zonal flow of $v_\theta^{n=0}$ because the radial force balance is satisfied as $E_r^{n=0} \approx v_\theta^{n=0} B_{\varphi 0} - v_\varphi^{n=0} B_{\theta 0}$.) The time evolution of the zonal flow is in synchronization with TM and finally becomes the dominant mode with the amplitude much larger than that of the $n = 1$ TAE and TM component, which is consistent with the kinetic energy evolution in figure 6.

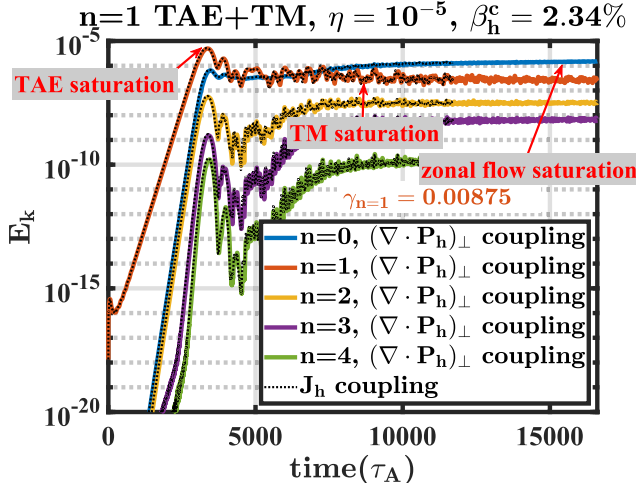


Figure 6. Time evolution of the kinetic energy for the simulation of the TAE + TM case. The saturation moments of the $n = 1$ TAE, $m/n = 2/1$ TM, and $n = 0$ zonal flow component are annotated. The result obtained from the pressure coupling scheme is plotted with colored solid lines, while that from the current coupling scheme is plotted with black dotted lines.

The mode structure of the zonal flow $E_r^{n=0}$ is shown in figure 11. The zonal flow is axisymmetric with the poloidal harmonics dominated by the $m = 0$ harmonic (see figure 11(b)). Besides, the direction of zonal flow reverses around the $q = 2$ surface. The $n = 0$ zonal flow is in ion (electron) diamagnetic drift direction inside (outside) the $q = 2$ rational surface. Note that in our simulations, the ion diamagnetic drift $v_{i*} = -(\nabla p_i \times \mathbf{B})/en_i B^2$ (n_i is the ion number density, and the subscript ‘i’ denotes quantities of ion) is negative in the poloidal section, because the radial component of ∇p_i is negative and B_φ is positive. For electrons, the diamagnetic drift is positive in the poloidal section. The reversal of zonal flow around the $q = 2$ rational surface suggests the important role played by the $m/n = 2/1$ TM in the generation of this dominant zonal flow. And the direction of zonal flow is mainly determined by the nonlinear magnetic tension force term in the right hand of the momentum equation, as will be illustrated in figure 15. The amplitude of $E_r^{n=0}$ inside the $q = 2$ rational surface is much larger than that outside the $q = 2$ rational surface. Nevertheless, the zonal flow has a global mode structure with a low radial shear, which results in a relatively weak inhibition effect on the TAE, as shown by figure 7(b). Therefore, in the TAE + TM case, three main branches of modes exist in the nonlinear stage, i.e. the $n = 1$ high-frequency TAE ($\omega_{\text{TAE}} \approx 0.053$), the $n = 1$ low-frequency TM ($\omega_{\text{TM}} \approx 0$), and the $n = 0$ zero-frequency zonal flow ($\omega_{\text{zonal flow}} = 0$). For the TAE, TM, and zonal flow, the matching condition of mode frequencies is not satisfied: $\omega_{\text{TAE}} - \omega_{\text{TM}} \neq \omega_{\text{zonal flow}}$, although the matching condition of mode numbers is satisfied: $n_{\text{TAE}} - n_{\text{TM}} = n_{\text{zonal flow}}$. Consequently, the $n = 0$ zonal flow is not directly generated by the nonlinear coupling between harmonics of the high-frequency TAE and the low-frequency TM.

Besides, we adopt the antenna ($\omega_{\text{ANT}} = 0.053$) in the CLT code to excite TAE without EPs but with the $m/n = 2/1$ TM (**the TAE (antenna) + TM case**). The mode structure of the antenna consisting of the $m = 2$ & 3 harmonics, is adopted from the linear stage of the pure TAE case with EPs, see figure 12(c). As shown by figure 12(a), the TAE excited by the antenna extends more outward, but the mode is truncated at $r \approx 0.4$ because of the continuum damping, which is significantly different from the TAE excited by EPs (a dominant $m = 2$ harmonic corresponding to the EPM branch at $r \approx 0.4$ is excited). The saturation amplitude of the $n = 0$ zonal component in the TAE (antenna) + TM case is much lower than that of the $n = 1$ component (see figure 12(b)). In addition, in the TAE + TM case (the TAE is excited by EPs), when we turn off EPs at $t = 10000$ in the CLT-K code, the dominant $n = 0$ zonal flow exponentially decays to a low level as shown in figure 13(a). Besides, without the driving effect of EPs after $t = 10000$, the $n = 1$ TAE oscillation vanishes quickly and the $n = 1$ component is dominated by TM, which is shown by the red line in figure 13(a) and the frequency spectrum in figure 13(b). Consequently, the generation and maintaining of the dominant $n = 0$ zonal flow require the co-existence of both TM and EPs.

We plot the distribution of the $n = 1$ component of the $(\nabla \cdot \delta \mathbf{P}_h)_\perp$ for the TAE + TM case after the saturation of the $n = 1$ TM in figure 14. In the presence of the saturated $m/n = 2/1$ magnetic island, a significant redistribution of EPs can be observed. The radial component $(\nabla \cdot \delta \mathbf{P}_h)_{\perp r}$ shows a large reversal around the $q = 2$ surface, corresponding to the radial redistribution of EPs by TM. The poloidal $(\nabla \cdot \delta \mathbf{P}_h)_{\perp \theta}$ and toroidal $(\nabla \cdot \delta \mathbf{P}_h)_{\perp \varphi}$ components show the obvious $m/n = 2/1$ structure, which is associated with the poloidal redistribution of EPs by TM. The structure of $(\nabla \cdot \delta \mathbf{P}_h)_\perp$ remains almost unchanged after TM begins to saturate (from $t \approx 7000$ to the end of the simulation, $t \approx 17000$). The persistent distribution of $(\nabla \cdot \delta \mathbf{P}_h)_\perp$ provides a steady $n = 1$ driving source on the momentum equation (equation (8)). Consequently, we extract the $n = 1$ component of $(\nabla \cdot \delta \mathbf{P}_h)_\perp$ at the end of the simulation ($t \approx 17000$) from the TAE + TM case, and put it in the momentum equation as a constant source term to carry out a pure TM simulation without EPs (**the $(\nabla \cdot \delta \mathbf{P}_h)_\perp + \text{TM}$ case**), that is, the momentum equation of equation (3) in the $(\nabla \cdot \delta \mathbf{P}_h)_\perp + \text{TM}$ case becomes as follow,

$$\begin{aligned} \partial_t \mathbf{v} = & -\mathbf{v} \cdot \nabla \mathbf{v} + [\mathbf{J} \times \mathbf{B} - \nabla p - (\nabla \cdot \delta \mathbf{P}_h)_\perp] / \rho \\ & + \nabla \cdot [\nu \nabla (\mathbf{v} - \mathbf{v}_0)]. \end{aligned} \quad (23)$$

Interestingly, with the co-existence of the $n = 1$ source term $(\nabla \cdot \delta \mathbf{P}_h)_\perp$ and the $m/n = 2/1$ TM, a strong $n = 0$ zonal flow component is generated as well without EPs as shown in figure 15(a).

To further understand the generation mechanism of the dominant $n = 0$ zonal component in the TAE + TM case, we list the linear and nonlinear terms related with the $n = 0$ component in the momentum equation (equation (8)), including *the nonlinear convective term* $\mathbf{C} = -\mathbf{v} \cdot \nabla \mathbf{v}$ (also known as the Reynolds stress), *the linear response term*

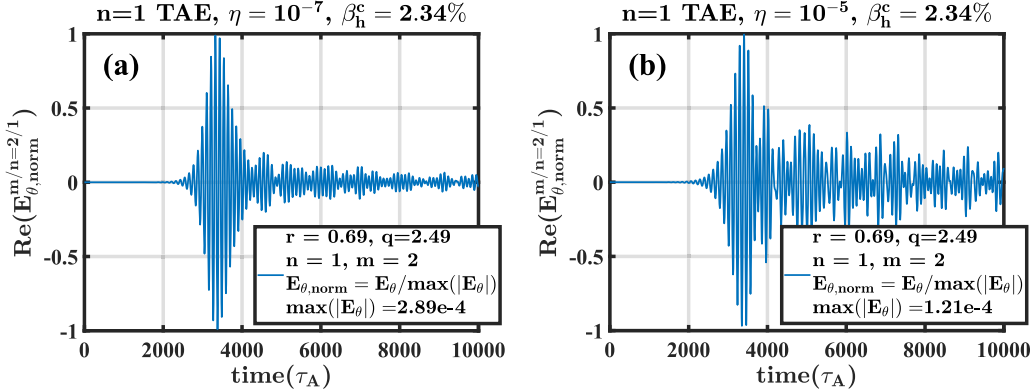


Figure 7. Time evolutions of the normalized real component of the poloidal electric field of the TAE ($E_{\theta,\text{norm}}^{m/n=2/1}$) at the $q = 2.49$ surface for (a) the pure TAE case and (b) the TAE + TM case. The poloidal electric field is normalized by its maximum value.

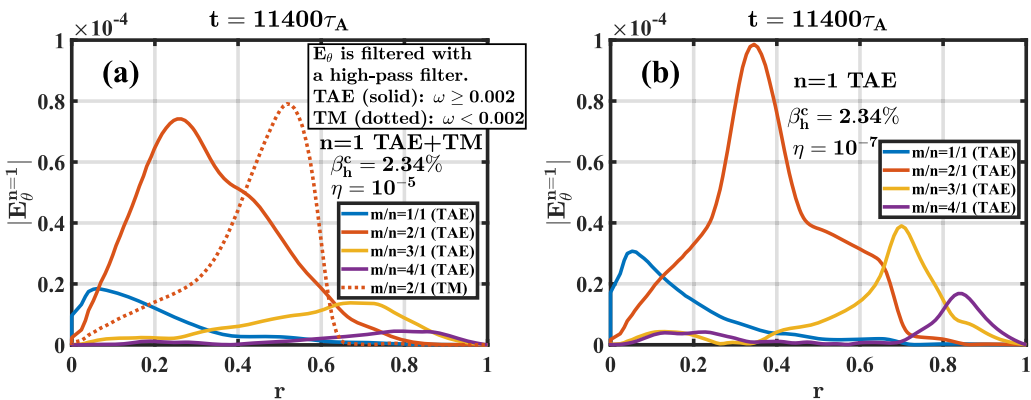


Figure 8. Radial mode structures of the $n = 1$ poloidal electric field E_{θ} at $t = 11400 \tau_A$ for (a) the TAE + TM case. [The TAE mode structure is separated out with a high-pass filter ($\omega \geq 0.002$), i.e. the remaining low-frequency ($\omega < 0.002$) component is dominated by the TM.] and (b) the pure TAE case. The solid lines in (a) and (b) represent the mode structures of the high-frequency TAE components, while the dotted line in (a) represents the $m = 2$ mode structure of the low-frequency TM component.

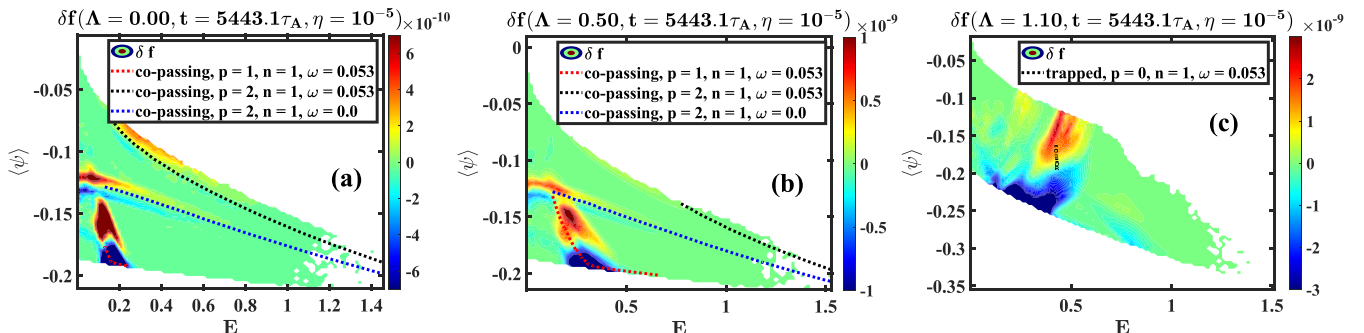


Figure 9. The δf structures of EPs for the TAE + TM case for different pitch angles (a) $\Lambda = 0.00$, (b) $\Lambda = 0.50$, and (c) $\Lambda = 1.10$. The resonance conditions between EPs and the modes are plotted with dotted lines.

$L = [\mathbf{J}_0 \times \delta \mathbf{B} + \delta \mathbf{J} \times \mathbf{B}_0 - (\nabla \cdot \delta \mathbf{P}_h)_\perp]/\rho$ (note that the term L is not exactly linear because the variation of plasma density ρ contributes a small nonlinear effect), the nonlinear magnetic tension force term $T = (\delta \mathbf{B} \cdot \nabla) \delta \mathbf{B}/\rho$ (also known as the Maxwell stress), the nonlinear magnetic pressure force term $P = -\nabla(\delta \mathbf{B}^2/2)/\rho$, and the viscous diffusion term $D = \nabla \cdot [\nu \nabla(\mathbf{v} - \mathbf{v}_0)]$ (note that the terms of T and P are separated from the nonlinear Lorentz force $(\delta \mathbf{J} \times \delta \mathbf{B})/\rho$).

The radial mode structures of the above different terms contributing to the growth/damping of the $m/n = 0/0$ zonal flow component are plotted in figure 15(b). The $m/n = 0/0$ component of the nonlinear convective term C mainly localizes around the $q = 2$ rational surface. The $m/n = 0/0$ component of the linear response term L has a wide radial distribution but the amplitude is weak inside the $q = 2$ rational surface. Importantly, the $m/n = 0/0$ component of the nonlinear

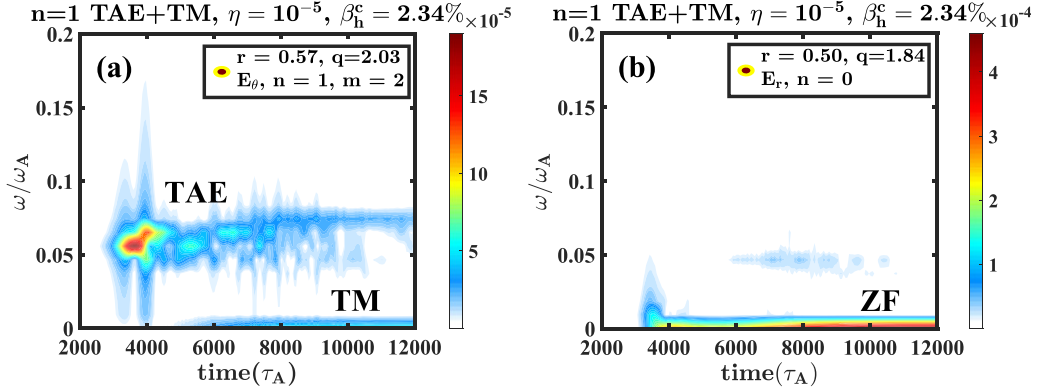


Figure 10. Mode frequencies of the TM + TAE case versus time for (a) the $m/n = 2/1$ poloidal electric field $E_{\theta}^{m/n=2/1}$, and (b) the $n = 0$ radial electric field $E_r^{n=0}$.

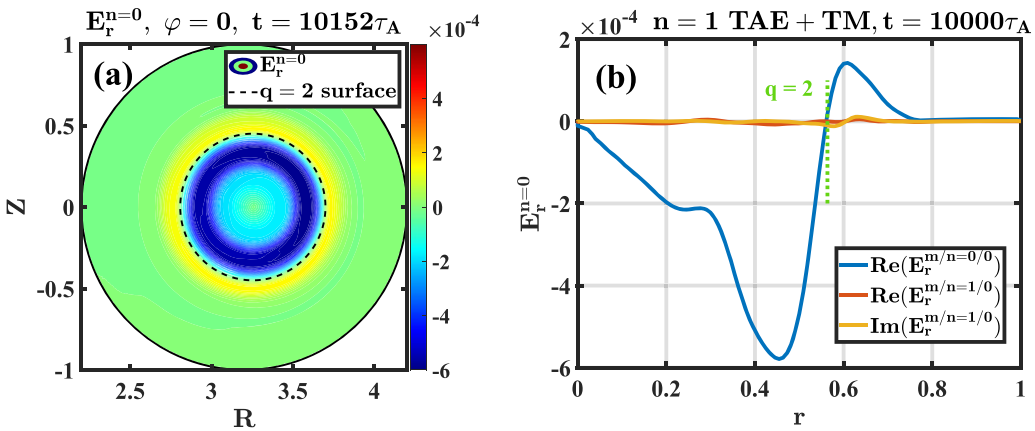


Figure 11. The radial electric field $E_r^{n=0}$ of the TAE + TM case: (a) the contour plot of $E_r^{n=0}$ and (b) the radial mode structures of the $m = 0$ & 1 harmonics of $E_r^{n=0}$. The location of the $q = 2$ rational surface is marked out.

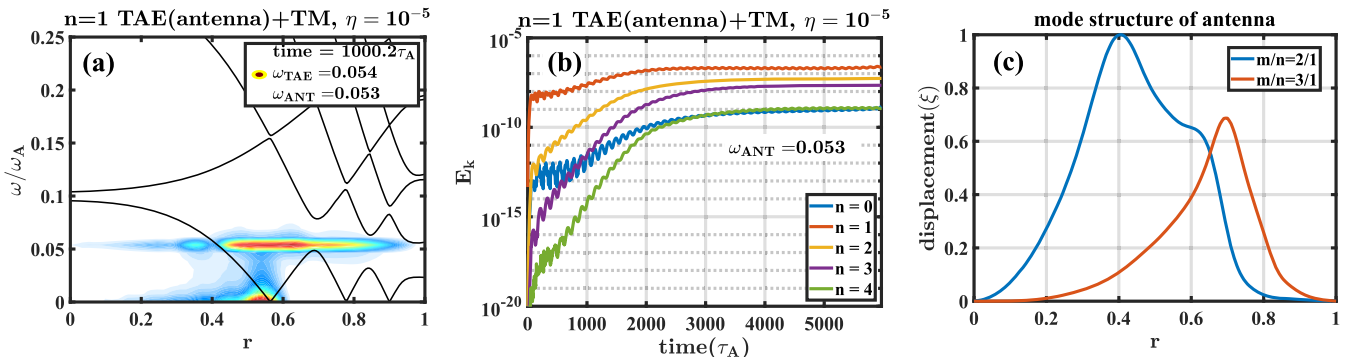


Figure 12. Simulation results for the TAE (antenna) + TM case: (a) mode frequencies of the $n = 1$ poloidal electric field with the $n = 1$ shear Alfvén continuum (solid lines), (b) time evolution of the kinetic energy, and (c) the mode structure of the antenna. Note that the mode structure of the antenna consisting of $m = 2$ & 3 harmonics, is adopted from the linear stage of the pure TAE case with EPs.

magnetic tension force term \mathbf{T} has a strong magnitude and ranges from the core region to the $q = 2$ rational surface. The $m/n = 0/0$ component of the nonlinear magnetic pressure force term \mathbf{P} is negligible compared with other terms. In addition, the $m/n = 0/0$ component of the viscous diffusion term \mathbf{D} mainly plays an obvious damping role in the evolution of the zonal flow. And the distribution of the viscous diffusion term

\mathbf{D} is determined by the profile of $m/n = 0/0$ zonal component. After summing all $m/n = 0/0$ component terms in the right hand of the momentum equation (equation (8)), as expected, the total $m/n = 0/0$ radial structure of all terms (black line in figure 15(b)) is almost the same as the $m/n = 0/0$ structure of $v_{\theta} * \gamma$ (red line in figure 15(b)), where the growth rate γ of $m/n = 0/0$ component of the poloidal flow v_{θ} is estimated

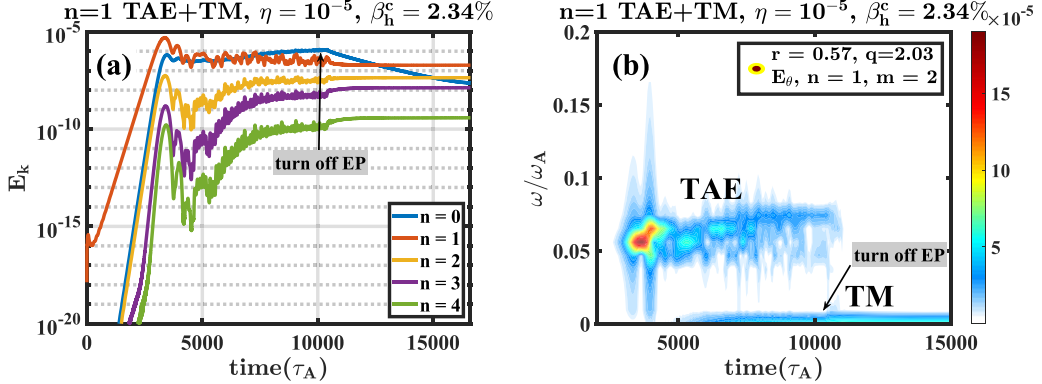


Figure 13. (a) Time evolution of the kinetic energy and (b) mode frequencies versus time for the TAE + TM case. EPs in the CLT-K code are turned off after $t = 10\,000$ in the simulation.

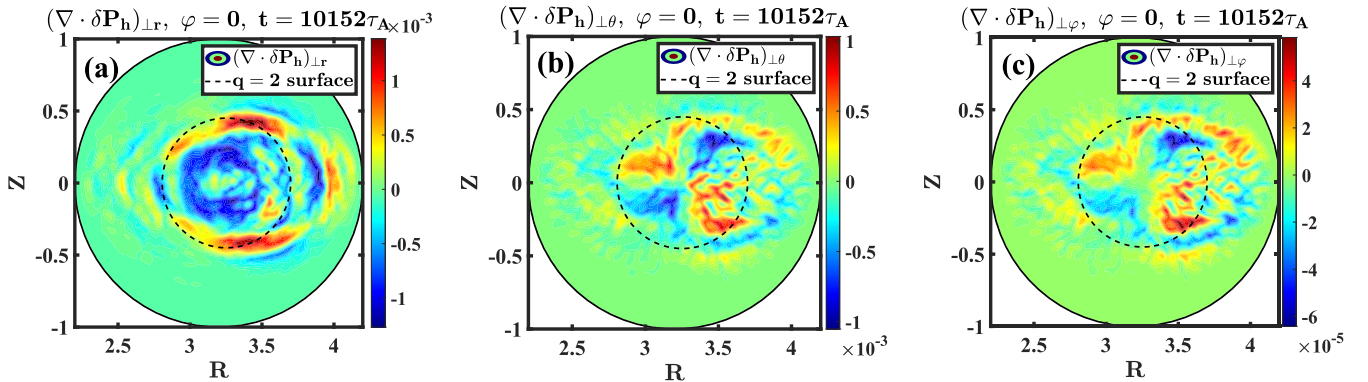


Figure 14. The spatial distribution of the $n = 1$ component of $(\nabla \cdot \delta \mathbf{P}_h)_{\perp}$ for the TAE + TM case after the saturation of the $n = 1$ TM: (a) the radial component $(\nabla \cdot \delta \mathbf{P}_h)_{\perp r}$, (b) the poloidal component $(\nabla \cdot \delta \mathbf{P}_h)_{\perp \theta}$, and (c) the toroidal component $(\nabla \cdot \delta \mathbf{P}_h)_{\perp \varphi}$.

to be 6.12×10^{-4} at $r \approx 0.5$. The slight difference between the black and red lines in figure 15(b) is caused by the variation of the growth rate γ of $m/n = 0/0$ v_θ component at different radial locations. Consequently, in the core region, the nonlinearity of the momentum equation, especially the nonlinear magnetic tension force term (the dotted yellow line in figure 15(b)) intensively drives the poloidal $m/n = 0/0$ zonal flow in the negative direction, corresponding to the direction of the ion-diamagnetic drift, which is consistent with the mode structure of $E_r^{n=0}$ in figure 11(b). The directions of the zonal flow and the nonlinear magnetic tension force term T are mainly determined by the redistributed $n = 1$ $(\nabla \cdot \delta \mathbf{P}_h)_{\perp}$ source term. The generation process of the dominant zonal flow can be described as: firstly, besides the $m/n = 2/1$ TM, the source term of $n = 1$ $(\nabla \cdot \delta \mathbf{P}_h)_{\perp}$ intensively drives $n = 1$ perturbations, including significant modifications on the magnetic field; secondly, through the nonlinear magnetic tension force term $T = (\delta \mathbf{B} \cdot \nabla) \delta \mathbf{B} / \rho$, the $n = 1$ perturbed magnetic field caused by both the redistributed $(\nabla \cdot \delta \mathbf{P}_h)_{\perp}$ term and the $m/n = 2/1$ TM nonlinearly produce the dominant driving effect on the zonal flow in the direction of ion-diamagnetic drift (inside the $q = 2$ rational surface); and finally, the zonal flow is saturated due to the balance between the nonlinear driving effects and the viscous damping effect. Nevertheless, the radial mode structure of $m/n = 0/0$ zonal flow of the $(\nabla \cdot \delta \mathbf{P}_h)_{\perp}$ +

TM case (see red line in figure 15(b)) is still slightly different from that of the TAE + TM case (see blue line in figure 11(b)), especially around the $q = 2$ rational surface, which may be caused by the lack of the TAE component and the fluctuation of $(\nabla \cdot \delta \mathbf{P}_h)_{\perp}$ term in the $(\nabla \cdot \delta \mathbf{P}_h)_{\perp}$ + TM case without EPs (figure 15). The generation mechanism of the zonal flow in the TAE + TM case is different from previous studies, which emphasize the importance of the radial orbit loss current of EPs J_{hr} on driving the zonal flow [22, 43]. In our simulations, the $n = 0$ component of \mathbf{J}_h is not included, i.e. the redistribution or orbit loss of EPs only directly drives the $n = 1$ perturbation, and the $n = 0$ zonal flow must be generated through the nonlinear coupling of the $n \neq 0$ harmonics.

Another interesting phenomenon worth further discussion is that the peak positions of the $m = 2$ EPM harmonic in figure 5(b) and the $n = 0$ zonal flow in figure 11(b) are both located at $r \approx 0.4$, which indicates that the strong $m = 2$ EPM harmonic might be a potential candidate that affects the generation mechanism and the mode structure of the dominant zonal flow. However, the exact roles of the $m = 2$ EPM harmonic in the EP redistribution and the zonal flow generation are hard to identify at present. According to the existing results and the above analyses, the $m/n = 2/1$ TM is distinctly necessary for the redistribution of EPs and the generation of the dominant zonal flow, and the $m = 2$ EPM branch seems to play a

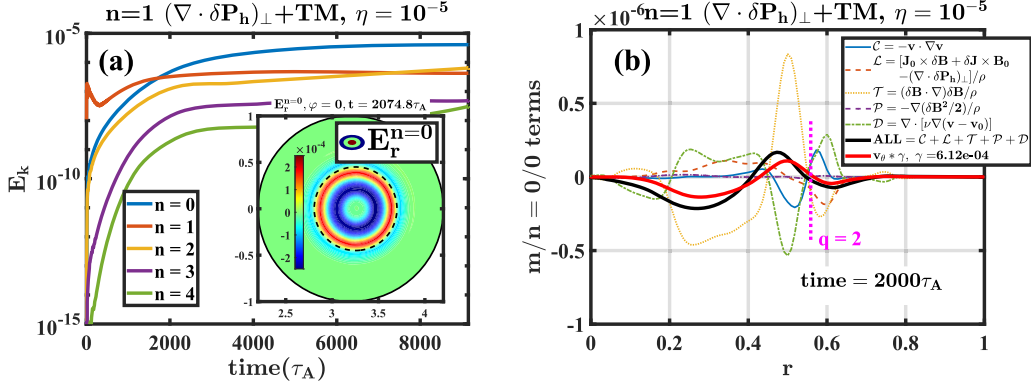


Figure 15. Simulation results for the $(\nabla \cdot \delta P_h)_\perp + \text{TM}$ case: (a) time evolution of the kinetic energy and the contour plot of $E_r^{n=0}$ at $t = 2074.8$, and (b) the $m/n = 0/0$ radial mode structures contributed from different terms in the momentum equation at $t = 2000$. The growth rate of the $m/n = 0/0$ component of the poloidal flow v_θ is estimated to be 6.12×10^{-4} at $r \approx 0.5$. The location of $q = 2$ rational surface is marked out.

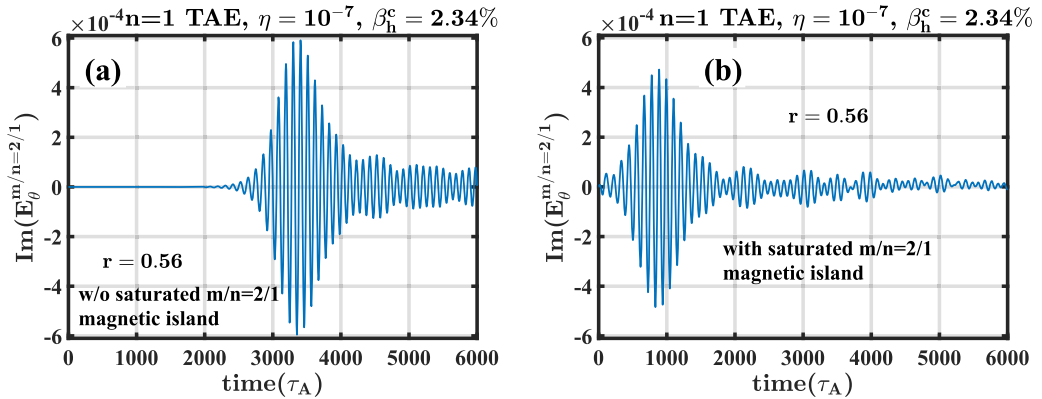


Figure 16. Time evolutions of the imaginary part of $E_\theta^{m/n=2/1}$ of the $n = 1$ TAE at $r = 0.56$ for (a) without the saturated $m/n = 2/1$ magnetic island, and (b) with the saturated $m/n = 2/1$ magnetic island. The simulation parameters are $\eta = 10^{-7}$ and $\beta_h^c = 2.34\%$. Without the saturated $m/n = 2/1$ magnetic island, the $n = 1$ TAE is originally unstable.

synergistic role together with the $m/n = 2/1$ TM in the processes of the EP redistribution and the zonal flow generation. To fully understand this issue, a further detailed study will be performed by adjusting the simulation conditions, including but not limited to the initial q -profile of the equilibrium, and the distribution profile of EPs so that a pure TAE without the $m = 2$ EPM component can be excited.

3.4. Influence of the $m/n = 2/1$ magnetic island on the excitation of the $n = 1$ TAE

In this subsection, we will briefly discuss the excitation behaviors of the $n = 1$ TAE in the presence of the $m/n = 2/1$ magnetic island. The saturated $m/n = 2/1$ magnetic island resulting from the pure TM case (including \mathbf{E} , \mathbf{B} , \mathbf{J} , ρ and \mathbf{v}) is artificially adopted as the initial equilibrium profile for the simulations, and then the isotropic EPs with the slowing down distribution function of equation (22) are loaded. The resistivity used in the simulation is $\eta = 10^{-7}$. Through a systematic scan of β_h^c , the unstable criteria for the $n = 1$ TAE with $\eta = 10^{-7}$ is found to be $\beta_h^c > 0.76\%$. Firstly, for an originally unstable TAE case ($\beta_h^c = 2.34\%$) without the saturated $m/n = 2/1$ magnetic island, it takes about $3500\tau_A$ for the TAE to reach

its maximum amplitude as shown in figure 16(a). However, as shown in figure 16(b), with the saturated $m/n = 2/1$ magnetic island, the TAE is immediately excited by EPs with a larger growth rate and reaches its maximum amplitude in the much earlier time around $t = 800$. On the other hand, for an originally stable TAE case ($\beta_h^c = 0.71\%$) without the saturated $m/n = 2/1$ magnetic island, the TAE is not excited and the mode amplitude maintains at the noise level in the whole simulation period as shown in figure 17(a). With the saturated $m/n = 2/1$ magnetic island, the originally stable TAE is found to be strongly destabilized and saturates at a relatively high level around $t = 1500$ as shown in figure 17(b). Therefore, the large $m/n = 2/1$ magnetic island can result in the burst of the originally unstable TAE and the destabilization of the originally stable TAE.

To understand the role played by the $m/n = 2/1$ magnetic island on the excitation of the TAE, the perturbed and total distribution function profiles for the originally stable TAE case with the saturated $m/n = 2/1$ magnetic island are plotted in figure 18. The significant $p = 2, n = 1$ TM resonance appears quickly with the $m/n = 2/1$ magnetic island (less than $300\tau_A$) as shown in figure 18(a), which corresponds to the radial

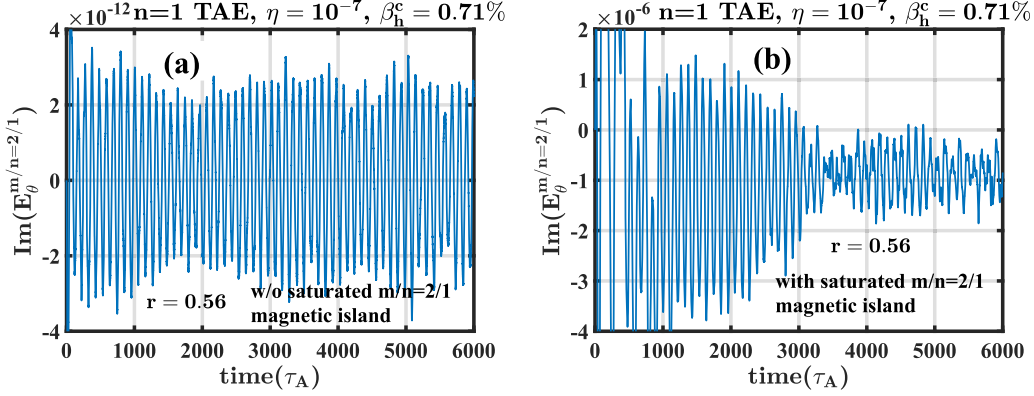


Figure 17. Time evolutions of the imaginary part of $E_\theta^{m/n=2/1}$ of the $n = 1$ TAE at $r = 0.56$ for (a) without the saturated $m/n = 2/1$ magnetic island and (b) with the saturated $m/n = 2/1$ magnetic island. The simulation parameters are $\eta = 10^{-7}$ and $\beta_h^c = 0.71\%$. Without the saturated $m/n = 2/1$ magnetic island, the $n = 1$ TAE is originally stable.

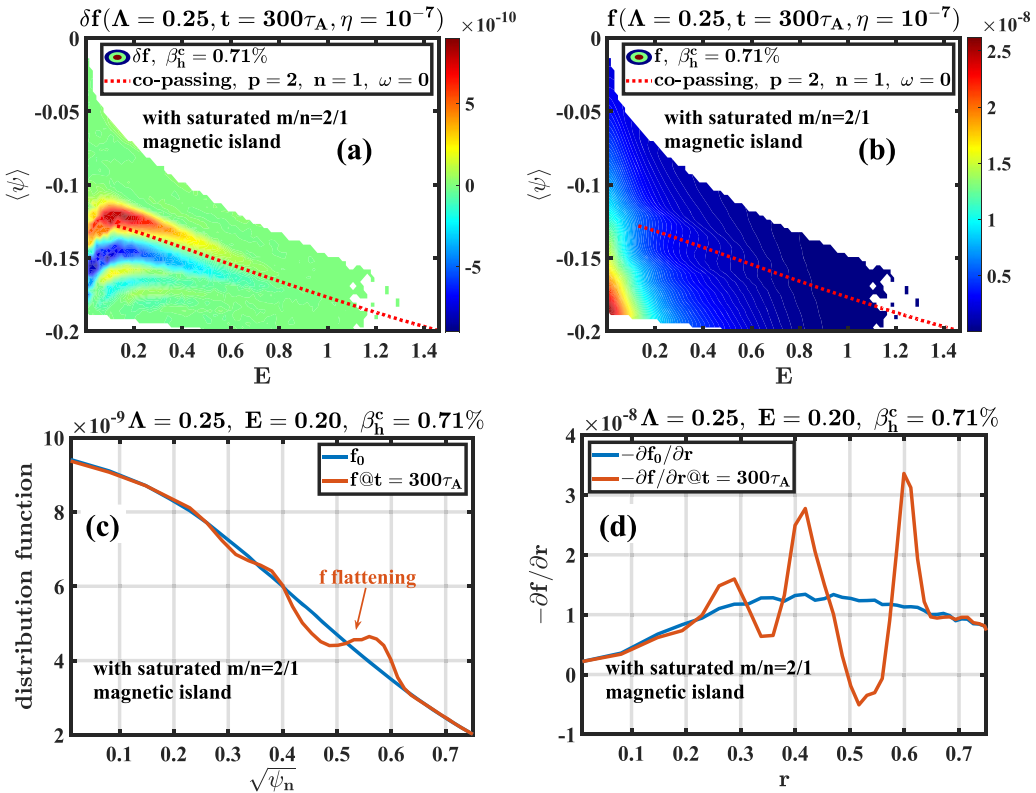


Figure 18. Distribution function profiles for the originally stable TAE case ($\eta = 10^{-7}$ and $\beta_h^c = 0.71\%$) with the saturated $m/n = 2/1$ magnetic island at $t = 300$. (a) The δf distribution ($\Lambda = 0.25$) with the $p = 2, n = 1$ TM resonance line plotted with the red-dotted line, (b) the f distribution ($\Lambda = 0.25$) with the $p = 2, n = 1$ TM resonance line plotted with the red-dotted line, (c) the radial f distribution (blue line for the initial profile and orange line for the profile at $t = 300$) at $\Lambda = 0.25$ and $E = 0.20$, and (d) the radial distribution of spatial gradients $\partial f / \partial r$ (blue line for the initial profile and orange line for the profile at $t = 300$) at $\Lambda = 0.25$ and $E = 0.20$.

redistribution of passing EPs. The $p = 2, n = 1$ TM resonance also results in the flattening of the EP distribution function around the $q = 2$ rational surface as shown by figures 18(b) and (c). As a result, as shown in figure 18(d), the spatial gradients of the redistributed EPs $\partial f / \partial r$ inside and outside the TM are almost doubled compared with their initial values. Since the growth rate of the TAE is proportional to the spatial gradient of the EP distribution function, $\gamma \propto \partial_E f|_{E'} = -f/T(1 - n\omega_*/\omega)$, where $\omega_* = qT/Z_h eB \bullet \partial_r \ln f$ [44], the

enhanced spatial gradient of redistributed EPs could be responsible for the burst or destabilization of the TAE.

4. Conclusion and discussion

In summary, in the presence of the $m/n = 2/1$ TM, the large amplitude zonal flow is easily to be generated due to the spatial redistribution of EPs by the $m/n = 2/1$ magnetic island. If the

$n = 1$ TAE saturates before TM takes place, the EP redistribution resulting from a large magnetic island directly gives rise to a strong zonal flow. However, if the EP redistribution by TM is prior to the excitation of TAE, the TM tends to result in the burst of originally unstable TAE or the destabilization of originally stable TAE in a quite short timescale (less than $2000\tau_A$). Besides, the saturated magnetic island width is independent of the resistivity. The enhanced zonal flow generation and the TAE excitation are mainly resulted from the EP redistribution by the $m/n = 2/1$ magnetic island. Thus, the value of the resistivity will mainly influence the time scale of the TM growth but has a limited influence on the final state of the system qualitatively. Nevertheless, the investigations on the quantitative parameter dependences on the resistivity, the viscosity, the geometry of tokamak, the initial equilibrium, the distribution profile & β_h of EPs, etc, will be carried out systematically in our future work.

In the pure TAE case, the growth rate of the zonal flow at the linear stage of the TAE is twice that of the pumping TAE, and its generation is attributed to the forced driven process of the pumping TAE [23, 24, 40]. The TAE-driven zonal flow dominated by $m = 0$ & 1 harmonics is mainly localized around the extreme point of the TAE harmonic and the accumulation point of the TAE gap [23, 40].

In the TAE + TM case, the significant $p = 2$ TM resonance of co-passing EPs is observed, which suggests that EPs are largely redistributed by the $m/n = 2/1$ magnetic islands. The EP distribution becomes flattened around the $p = 2$ TM resonance line, and the spatial gradient of the EP distribution is almost twice its initial value at the edge of the magnetic island, which accounts for the burst or destabilization of TAE with a large $m/n = 2/1$ magnetic island. With TM, the amplitude of TAE shows a slower decay after reaching its maximum, and the mode structure is dominated by the $m = 2$ harmonic. With the co-existence of EPs/TAE and TM, the $n = 0$ zonal flow gradually becomes dominant when TM grows up, with a global and strong $m = 0$ component in the ion-diamagnetic drift direction inside the $q = 2$ rational surface. The nonlinear generation mechanism of the dominant zonal flow in the TAE + TM case is attributed to the driving effect of the redistributed $n = 1$ ($\nabla \cdot \delta \mathbf{P}_h$) $_{\perp}$ and the MHD nonlinearity. The $m/n = 2/1$ TM is essential for the redistribution of EPs and the generation of the dominant zonal flow. Further systematic studies are needed and will be conducted to figure out the potentially synergistic effect of the $m = 2$ EPM branch on the EP redistribution and the zonal flow generation.

On account of the important roles of zonal flows in TAE saturation and drift-wave turbulence modulation, and considering the universality of TAE/EPs and TM activities in tokamaks, the nonlinear generation of a strong zonal flow by TAE/EPs [45, 46] and TM could be a potential candidate mechanism for the phenomena of internal transport barrier and improvement of plasma confinement [47–49].

Acknowledgments

The authors would like to acknowledge Professor L. Chen and W. Chen for helpful discussions. This work is supported by the National Natural Science Foundation of China under Grant No. 11835010 and 11775188, Fundamental Research Fund for Chinese Central Universities, and National Key R & D Program of China under Grant No. 2019YFE03020003.

ORCID iDs

H.W. Zhang  <https://orcid.org/0000-0003-1342-5756>
Z.W. Ma  <https://orcid.org/0000-0001-6199-9389>
Z.Y. Qiu  <https://orcid.org/0000-0002-7548-8819>

References

- [1] Todo Y. 2019 *Rev. Mod. Plasma Phys.* **3** 1
- [2] Cheng C.Z. and Chance M.S. 1986 *Phys. Fluids* **29** 3695
- [3] Cheng C.Z., Chen L. and Chance M.S. 1985 *Ann. Phys., NY* **161** 21
- [4] Cai H., Wang S., Xu Y., Cao J. and Li D. 2011 *Phys. Rev. Lett.* **106** 075002
- [5] Cai H. and Fu G. 2012 *Phys. Plasmas* **19** 072506
- [6] Takahashi R., Brennan D.P. and Kim C.C. 2009 *Phys. Rev. Lett.* **102** 135001
- [7] Gao B., Cai H., Wang F., Gao X. and Wan Y. 2021 *Phys. Plasmas* **28** 012104
- [8] Zhu X.-L., Chen W., Wang F. and Wang Z.-X. 2020 *Nucl. Fusion* **60** 046023
- [9] Chen W. *et al* 2019 *Nucl. Fusion* **59** 096037
- [10] Buratti P., Smeulders P., Zonca F., Annibaldi S.V., De Benedetti M., Kroegler H., Regnoli G. and Tudisco O. (FTU-Team) 2005 *Nucl. Fusion* **45** 1446
- [11] Hole M.J. and Appel L.C. 2009 *Plasma Phys. Control. Fusion* **51** 045002
- [12] Chen W. *et al* 2014 *Europhys. Lett.* **107** 25001
- [13] Shi P.W. *et al* 2017 *Phys. Plasmas* **24** 042509
- [14] Chen W. *et al* 2017 *Nucl. Fusion* **57** 114003
- [15] Liu L., He J., Hu Q. and Zhuang G. 2015 *Plasma Phys. Control. Fusion* **57** 065007
- [16] Shi P.W. *et al* 2019 *Nucl. Fusion* **59** 086001
- [17] Zhu J., Ma Z.W., Wang S. and Zhang W. 2018 *Nucl. Fusion* **58** 046019
- [18] Lin Z., Hahm T.S., Lee W.W., Tang W.M. and White R.B. 1998 *Science* **281** 1835
- [19] Chen L., Lin Z. and White R. 2000 *Phys. Plasmas* **7** 3129
- [20] Diamond P.H., Itoh S.-I., Itoh K. and Hahm T.S. 2005 *Plasma Phys. Control. Fusion* **47** R35
- [21] Itoh K., Itoh S.-I., Diamond P.H., Hahm T.S., Fujisawa A., Tynan G.R., Yagi M. and Nagashima Y. 2006 *Phys. Plasmas* **13** 055502
- [22] Ohshima S. *et al* 2007 *Plasma Phys. Control. Fusion* **49** 1945
- [23] Todo Y., Berk H.L. and Breizman B.N. 2010 *Nucl. Fusion* **50** 084016
- [24] Qiu Z., Chen L. and Zonca F. 2016 *Phys. Plasmas* **23** 090702
- [25] Wang S., Ma Z.W. and Zhang W. 2016 *Phys. Plasmas* **23** 052503
- [26] Wang Z., Lin Z., Deng W., Holod I., Heidbrink W.W., Xiao Y., Zhang H., Zhang W. and Van Zeeland M. 2015 *Phys. Plasmas* **22** 022509
- [27] Zhang H.W., Lin X., Ma Z.W., Zhang W. and Bagwell T.E. 2021 *Plasma Phys. Control. Fusion* **63** 035011
- [28] Zhang H.W., Ma Z.W., Zhang W., Sun Y.W. and Yang X. 2019 *Phys. Plasmas* **26** 112502

- [29] Zhang H.W., Zhu J., Ma Z.W., Kan G.Y., Wang X. and Zhang W. 2019 *Int. J. Comput. Fluid Dynam.* **33** 393
- [30] Zhang W., Ma Z.W. and Wang S. 2017 *Phys. Plasmas* **24** 102510
- [31] Zhu J., Ma Z. and Wang S. 2016 *Phys. Plasmas* **23** 122506
- [32] Zhang W., Jardin S.C., Ma Z.W., Kleiner A. and Zhang H.W. 2021 *Comput. Phys. Commun.* **269** 108134
- [33] Park W. *et al* 1992 *Phys. Fluids B* **4** 2033
- [34] Cary J.R. and Brizard A.J. 2009 *Rev. Mod. Phys.* **81** 693
- [35] Chew G.F., Goldberger M.L., Low F.E. and Chandrasekhar S. 1956 *Proc. R. Soc. A* **236** 112
- [36] Hu G. and Krommes J.A. 1994 *Phys. Plasmas* **1** 863
- [37] Parker S.E. and Lee W.W. 1993 *Phys. Fluids B* **5** 77
- [38] DeLucia J., Jardin S.C. and Todd A.M.M. 1980 *J. Comput. Phys.* **37** 183
- [39] Hegna C.C. and Callen J.D. 1994 *Phys. Plasmas* **1** 2308
- [40] Todo Y., Berk H.L. and Breizman B.N. 2012 *Nucl. Fusion* **52** 094018
- [41] Fu G.Y. and Park W. 1995 *Phys. Rev. Lett.* **74** 1594
- [42] Heidbrink W.W. 2008 *Phys. Plasmas* **15** 055501
- [43] Chen W., Xu Y., Ding X.T., Shi Z.B., Jiang M., Zhong W.L. and Ji X.Q. 2016 *Nucl. Fusion* **56** 044001
- [44] Todo Y. 2012 *AIP Conf. Proc.* **1478** 141
- [45] Di Siena A., Görler T., Poli E., Navarro A.B., Biancalani A. and Jenko F. 2019 *Nucl. Fusion* **59** 124001
- [46] Mazzi S. *et al* 2020 arXiv:2010.07977
- [47] Austin M.E. *et al* 2006 *Phys. Plasmas* **13** 082502
- [48] Joffrin E. *et al* 2003 *Nucl. Fusion* **43** 1167
- [49] Maget P. *et al* 2006 *Nucl. Fusion* **46** 797